1 # Aerosol formation and growth rates from chamber experiments
2 # using Kalman smoothing

3 Matthew Ozon[1], Dominik Stolzenburg[2], Lubna Dada[2], Aku Seppänen[1] and Kari E.J. Lehtinen[1,3]

4 [1] Department of Applied Physics, University of Eastern Finland, Kuopio, Finland
5 [2] Institute for Atmospheric and Earth System Research/ Physics, University of Helsinki, 00014 Helsinki, Finland
6 [3] Atmospheric Research Centre of Eastern Finland, Finnish Meteorological Institute, Kuopio, Finland
7

8 *Correspondence to*: Kari E.J. Lehtinen (kari.lehtinen@uef.fi)

11 **Abstract.**

12 Bayesian state estimation in the form of Kalman smoothing was applied to Differential Mobility Analyser Train (DMA-
13 train) measurements of aerosol size distribution dynamics. Four experiments were analysed in order to estimate the aerosol
14 size distribution, formation rate and size-dependent growth rate, as functions of time. The first analysed case was a
15 synthetic one, generated by a detailed aerosol dynamics model, and the other three chamber experiments performed at the
16 CERN CLOUD facility. The estimated formation and growth rates were compared with other methods used earlier for
17 the CLOUD data and with the true values for the computer-generated synthetic experiment. The agreement in the growth
18 rates was remarkably good for all studied cases. The formation rates matched also well, especially considering the fact
19 that they were estimated from data given by two different instruments, the other being the Particle Size magnifier (PSM).
20 The presented Fixed Interval Kalman Smoother (FIKS) method has clear advantages compared with earlier methods that
21 have been applied to this kind of data. First, FIKS can reconstruct the size distribution between possible size gaps in the
22 measurement in such a way that it is consistent with aerosol size distribution dynamics theory, and second, the method
23 gives rise to direct and reliable estimation of size distribution and process rate uncertainties if the uncertainties in the
24 kernel functions and numerical models are known.

25 **1   Introduction**

26 Atmospheric new particle formation and growth are important phenomena when considering global aerosol
27 concentrations. Their concentration together with their size distribution and chemical composition determines how
28 aerosols affect visibility, health and climate (Albrecht, 1989; Appel et al., 1985; Daellenbach et al., 2020; Pope and
29 Dockery, 2006; Twomey, 1974). These are determined by atmospheric dynamics and aerosol dynamics such as new
30 particle formation and growth as well as removal rates. Nieminen et al. (2018) reviewed the existing literature on the
31 formation and growth rates ranging from polar sites, with very small aerosol concentrations to polluted urban sites with
32 extremely high concentrations. The rates have been typically estimated using the methodology reviewed in Kulmala et
33 al. (2012), based on rather simple regression or balance equation approaches, suffering from potentially crude
34 approximations and permitting no proper estimation of the uncertainties. At the same time, however, instrument
35 development, especially advances in particle detection efficiency and mass spectrometry, has developed rapidly

36 (Kangasluoma et al., 2020). Potentially superior advanced data analysis methods have not been used, and, it is likely that
37 there are significant inaccuracies in the estimated particle formation and growth rates estimated previously (Kürten et al.,
38 2018).

39 There have been some attempts to estimate aerosol formation and growth rates with different inverse methods (Henze et
40 al., 2004; Kuang et al., 2012; Lehtinen et al., 2004; Sandu et al., 2005; Verheggen and Mozurkewich, 2006; Viskari et al.,
41 2012). We are, however, not aware of any of the above-mentioned methodology being used widely. The most promising
42 ones in our view, that include also estimations of uncertainties, have been the ones by Kupiainen-Määttä (2016) and
43 Shcherbacheva et al. (2020), who used Markov Chain Monte Carlo methodology to estimate evaporation rates as well as
44 their uncertainties from synthetic cluster dynamics data. In addition, the INSIDE-method by Pichelstorfer et al. (2018),
45 which is based on numerical solution of the aerosol general dynamic equation and matching the solution optimally to
46 integrated measured concentrations of selected size intervals, has been successfully applied to determining growth rates
47 at the CLOUD (Cosmics Leaving OUtdoor Droplets) experiments at CERN (European Organization for Nuclear
48 Research) (Stolzenburg et al., 2020). Furthermore, the results in very recent manuscript by McGuffin et al. (2020), in
49 which nucleation, growth and emission rates of are estimated using techniques from the field of nonlinear process control,
50 seem promising.

51 In a recent paper, Ozon et al. (2020) presented BAYROSOL, a Julia software package that combines a finite difference
52 solution to the general dynamic equation for aerosols (GDE; Seinfeld and Pandis, 2016) to Bayesian state estimation in
53 order to estimate unknown size dependent process rates (nucleation, condensation, losses) from known time evolution of
54 the aerosol size distribution. Using synthetic SMPS measurements Ozon et al., (2020) showed that the Fixed Interval
55 Kalman Smoother (FIKS; Kaipio and Somersalo, 2005) performed very well in estimating the process rates of the GDE
56 in two distinct cases. First in a case in which continuous nucleation, growth and losses lead to a nearly steady state size
57 distribution and second also in a case in which there is a growing nucleation mode after a nucleation burst. In the method,
58 the unknowns (such as the discretized particle size distribution) are modeled as random variables, and their prior
59 probability distributions are incorporated in the solution of the inverse problem. One important key feature of the Kalman
60 smoother method is that it estimates also the error covariance matrices of the process rates that is their uncertainties, if
61 the uncertainties of the measurement device are known.

62 In this manuscript, we show results of applying BAYROSOL, for the first time to real experimental data. We use
63 experiments performed with the differential mobility analyser-train (DMA-train; Stolzenburg et al., 2017) measuring
64 new particle formation and growth at the CERN CLOUD chamber (Duplissy et al., 2016; Kirkby et al., 2011). In addition
65 to testing the method with synthetic DMA-train data (in which the 'correct' results are known), we estimate formation
66 and growth rates from three different formation and growth experiments: sulphuric-ammonia (Stolzenburg et al., 2020),
67 alpha-pinene ozonolysis (Heinritzi et al., 2020) and iodic acid (He et al., 2021; Sipilä et al., 2016). We compare the
68 formation rates with results obtained by using the methodology by Dada et al. (2020) based on Particle Size Magnifier
69 (PSM) measurements and the growth rates with the results obtained by the INSIDE method (Pichelstorfer et al., 2018).
70 We chose the DMA-train measurements for three main reasons: the high time resolution makes it an ideal instrument for
71 nucleation studies, the collection efficiencies of the channels have been carefully characterized (Stolzenburg et al., 2017;
72 Wlasits et al., 2020) and finally, the data from this instrument has not been used to estimate directly particle formation
73 rates so far.

Atmospheric
Chemistry
and Physics
Discussions

2   Bayesian framework for parameter estimation

2.1   Aerosol measurement and evolution models

The quantities of interest in chamber experiments studying new particle formation are the particle number size-distribution, the formation rate at the critical cluster size and the growth rate of the freshly formed particles. The available measurements to infer these quantities usually size classify the aerosol and measure the size classified number concentrations. While the retrieval of the particle number size distribution from such measurements is a classical inverse problem (Chambolle and Pock, 2011; Kandlikar and Ramachandran, 1999; Wolfenbarger and Seinfeld, 1990), the estimation of the process parameters (formation and growth rate) is often done by analysis of the time evolution of the retrieved particle size distribution. Here, we focus on the formulation of the problem within a statistical Bayesian framework, where the state parameters described by a measurement model and an evolution model are treated as multivariate random processes and are estimated from measurements using a FIKS (Ozon et al., 2020).

A measurement can be described by a vector y^k representing m indirect observations (channels of the instrument) of the particle size distribution $n(d_p, t_k)$. The observations are linked to the size distribution by the so-called instrument transfer (or kernel) functions $\mathcal{H}$ such that:

$$y^k = \int \mathcal{H}(d_p) n(d_p, t_k) dd_p \tag{1}$$

The transfer functions $\mathcal{H}$ can be inferred from calibration experiments and instrument design considerations. Direct inversion of Eq. (1) for every time instant t_k is typically an underdetermined and ill-posed inverse problem and requires some additional assumptions in order to avoid oscillatory and unstable solutions (Kandlikar and Ramachandran, 1999). At the same time, the time evolution of the particle size-distribution $n(d_p, t)$ can be described by the aerosol general dynamic equation (GDE):

$$\frac{\partial n}{\partial t}(d_p, t) = -\frac{\partial g(d_p, t) n(d_p, t)}{\partial d_p} - \lambda(d_p, t) n(d_p, t) - \text{CoagSink}(\beta, d_p, t) + \text{CoagSrc}(\beta, d_p, t) \tag{2}$$

Here, $g(d_p, t)$ is the condensation growth/evaporation rate, $\lambda(d_p, t)$ is the particle loss by deposition or dilution and CoagSink and CoagSrc are the sink and source rates due to particle coagulation within the size distribution with the coagulation coefficients β. An exact expression of all terms can be found in e.g. Ozon et al. (2020) and Seinfeld and Pandis (2016). The boundary conditions of Eq. (2) are given by the apparent formation rate $J_{d_{min}}(t) = g(d_{min}, t) n(d_{min}, t)$ of newly formed particles at the minimum detectable size d_{min} and a zero numerical flux condition $g(d_\infty, t) n(d_\infty, t) = 0$ at very large sizes. Altogether, the process parameters $g(d_p, t), J(t), \lambda(d_p, t)$ and $\beta(d_i, d_j)$ as well as the initial and boundary conditions determine completely the evolution of the size distribution, but especially $g(d_p, t)$ and $J(t)$ are usually not known. The coagulation coefficients $\beta(d_i, d_j)$ can often be obtained from theory (and coagulation can be even neglected in many applications with low particle concentrations) and the loss parameters $\lambda(d_p, t)$ are well quantified for controlled aerosol chamber experiments.

A single measurement of the size distribution y^k does not depend explicitly on the process parameters, but as $g(d_p, t)$ and $J(t)$ determine the temporal evolution of $n(d_p, t_k)$ the estimation of the process parameters is feasible from a sequence of l measurements y^k at several time instances.

Atmospheric
Chemistry
and Physics
Discussions

2.2 State estimation with Kalman smoothing

Following Ozon et al. (2020) we formulate the problem as a Bayesian state estimation problem. After discretization of the problem in size space ($i = 1, .., q$) and time ($k = 1, ... l$), we can define the state variable $X^k = [N_i^k \quad g_i^k \quad \lambda_i^k \quad J^k]$ for each time step k with the particle concentrations N_i^k per size discretization bin i, the condensation and loss terms g_i^k and λ_i^k, respectively, for each size discretization bin i and the nucleation rate J^k. The problem can then be formulated as:

$$X^{k+1} = F(X^k) + w^k \tag{3}$$

$$y^k = HX^k + v^k \tag{4}$$

Eq. (3) represents the discretized non-linear evolution model, which is based on the general dynamic equation for N^k, on second order processes for g^k and J^k, and a random walk evolution for λ^k (see Section 2.3). Eq. (4) represents the discretized linear observation model. The incorporation of positivity constraints for the process rates and the aforementioned second order models require minor modifications in the definition of the state variable X^k. This, however, does not cause any changes in the form of the state-space model (3)-(4). For the details on the above modifications as well as discretization of the GDE model, we refer to Ozon et al. (2020). The terms w^k and v^k are the error terms, which are approximated as normally distributed $\mathcal{N}(0, \Gamma_w^k)$ and $\mathcal{N}(0, \Gamma_e^k)$ with the covariance matrices Γ_w^k, Γ_v^k, which not only include stochastic noise, but also errors due discretization, model and parameter uncertainties. The GDE, i.e. the non-linear evolution model for N^k (Eq. (2)), is similar to an advection equation. Therefore, its numerical discretization schemes are often unstable and must be treated carefully to avoid oscillation and divergence or to minimize numerical diffusion (Shen et al., 2007; Smolarkiewicz, 1984). Thus, we show detailed considerations on the magnitude of the different error terms in the Supplement.

Algorithm 1 Extended Kalman Filter (EKF)	**Algorithm 2** Fixed Interval Kalman Smoother (FIKS)
Initial state: Expectation $X^{0\|0}$ and covariance $\Gamma^{0\|0}$	**Initialization:** Run Algorithm 1, store all variables
for $k = 1, \ldots, l$	**for** $k = l-1, \ldots, 1$
Prediction: expectation and covariance	Backward gain matrix
$X^{k\|k-1} = F(X^{k-1\|k-1})$	$A^k = \Gamma^{k\|k}(\partial F)^T (\Gamma^{k+1\|k})^{-1}$
$\Gamma^{k\|k-1} = \partial F^{k-1} \Gamma^{k-1\|k-1} (\partial F^{k-1})^T + \Gamma_w^{k-1}$	Smoother expectation and covariance
Kalman gain matrix:	$X^{k\|K} = X^{k\|k} + A^k(X^{k+1\|K} - X^{k+1\|k})$
$K^k = \Gamma^{k\|k-1}(H^k)^T (H^k \Gamma^{k\|k-1}(H^k)^T + \Gamma_v^k)^{-1}$	$\Gamma^{k\|K} = \Gamma^{k\|k} + A^k(\Gamma^{k+1\|K} - \Gamma^{k+1\|k})(A^k)^T$
Measurement update: filter expectation and covariance	**end**
$X^{k\|k} = X^{k\|k-1} + K^k(Y^k - H^k X^{k\|k-1})$	
$\Gamma^{k\|k} = (I - K^k H^k)\Gamma^{k\|k-1}$	
end	

Table 1: Extended Kalman Filter and Fixed Interval Kalman Smoother algorithms for estimation of the state variables and their variances X^k and Γ^k.

Atmospheric
Chemistry
and Physics
Discussions
Open Access
EGU

130 Considering this structure of the problem, a non-linear extension to the Kalman Filter (Extended Kalman Filter; EKF) is

131 a well suited algorithm for solving the unknown size-distribution and process parameters (Gelb, 1974; Kaipio and

132 Somersalo, 2005). It is a two stage recursive procedure, where in the first stage the future state and propagation of error

133 is predicted based on the state evolution model (Eq. (3)). In the second stage, the state variable and its covariance are

134 estimated by updating the predicted state variable and covariance. This so-called measurement update accounts for the

135 discrepancy between the realized measurements at time t_k and modelled measurements corresponding to the predicted

136 state variable. This procedure is repeated until the final measurement $k = l$. After finishing the EKF recursions, we utilize

137 a Fixed Interval Kalman Smoother (FIKS), which consists of a backward recursion from a backward gain matrix and

138 smooths the results by backwards recursion from l to 1. The workflow of the EKF and FIKS are illustrated in Table 1 and

139 more details on this algorithm can also be found in Ozon et al. (2020).

140 **2.3   Adaption to chamber experiments**

141 The state space model has been adjusted to represent best the evolution of an aerosol system during new particle formation

142 experiments in an atmospheric simulation chamber like CLOUD. For the time evolution of the process parameters, we

143 assume a rather smooth evolution for the nucleation and growth rates, approximated by a second order process (Ozon et

144 al., 2020):

145 $$J^{k+1} = (r_1 + r_2)J^k - r_1 r_2 J^{k-1} + w_J^k \qquad (5)$$

146 $$g^{k+1} = (r_1 + r_2)g^k - r_1 r_2 g^{k-1} + w_g^k \qquad (6)$$

147 The constants r_1, r_2 depend on the characteristic time of change, discretization time and a dampening factor and their

148 definition can be taken from (Ozon et al., 2020) and the corresponding values for our experiments are listed in Table S1

149 in the Supplement. The loss rates do not depend on time, in the chamber experiments of interest, and are well characterized

150 by dedicated wall loss experiments (Stolzenburg et al., 2020). .The dilution time of the chamber $\tau_{dil} = Q_{tot}/V_{chamber}$.

151 The time evolution is described by a random walk with a small stochastic noise term w_λ^k, and the expectation of the initial

152 state is set to the experimentally determined value with a standard deviation of $\pm 10\%$:

153 $$\lambda^{k+1} = \lambda^k + w_\lambda^k \qquad (7)$$

154 For fully defining the problem (Eq. (3)-(4)), an estimate of the covariance matrices corresponding to the error terms v^k

155 and w^k is needed. The definition of the covariance matrices corresponding to the state noise w^k on the size-distribution

156 evolution w_N^k, the growth rate w_g^k, the formation rate w_J^k and the wall loss rate w_λ^k follow the consideration of Ozon et al.

157 (2020). The covariances of the wall losses, the growth rate and the size-distribution are dominantly diagonal with some

158 additional off-diagonal terms in order to account for a correlation in size. The formulation given by Ozon et al. (2020)

159 was slightly altered to give a stronger correlation between the closest size bins (values for the different experiments are

160 given in Table S1 in the Supplement):

161 $$\Gamma_{N/g/\lambda}^k(i,j) = \sigma_{i,N/\lambda/g}\sigma_{j,N/\lambda/g} \, \exp\left(-\left(\frac{i-j}{\delta_{N/\lambda/g}}\right)^{a_{N/\lambda/g}}\right) \qquad (8)$$

162 For the size-distribution evolution, we find that $\sigma_{i,N}^2 = (\delta^k)^2 \text{Var}(W_i^k)$, with δ^k the discretization time-step and W_i^k the

163 error of the discretization of the size-distribution evolution. A detailed derivation of W_i^k is given in the Supplement.

164 The modelling error of the observation model and the measurement noise both contributing to v^k are assumed to be

165 mutually independent. For this reason, the covariance of the error term Γ_v^k in the measurement model is written as a sum

166 of the covariances of these two random variables, i.e. $\Gamma_v^k = \Gamma_{mod}^k + \Gamma_y^k$. For a detailed derivation we refer to the

167 Supplement, where we also show that the discretization error is negligible compared to model and measurement error if

168   a fine enough size discretization is chosen. We approximate Γ_v^k with uncorrelated processes, and hence the covariance

169   matrices are of the diagonal form. For the measurement error, the variance is given by Poisson counting statistics in the

170   case of a single-particle counting detector such as a condensational particle counter (CPC):

171    $$\Gamma_y^k(i, i) = y^k(i) \tag{9}$$

172   For the model uncertainty, we assume the variance of the kernel $\text{Var}(\Delta H_{i,j})$ is composed of an uncertainty proportional

173   to $H_{i,j}$ (for example due to an offset in the absolute calibration of the instrument) and a shifting size information error (for

174   example discrepancy between set and actual classified size in a mobility spectrometer). It can then be formulated as

175   (detailed values for the experiments under investigation can be found in Table S1 in the Supplement):

176    $$\Gamma_{mod}^k(i, i) = \sum_{j=1}^{q} \left(n(d_j)\Delta_j\right)^2 \text{Var}(\Delta H_{i,j}) \tag{10}$$

177   **3   Experimental methods**

178   We use experimental data from the CERN CLOUD experiment (Duplissy et al., 2016; Kirkby et al., 2011) where we

179   measured particle size-distributions in the sub-10 nm range with a DMA-train (Stolzenburg et al., 2017). The raw data

180   obtained from the DMA-train is used as input for the analysis of three different sets of experiments performed in the

181   atmospheric simulation chamber. The DMA-train instrument kernels are also used for modelling an instrument response

182   to simulated size-distribution data in order to verify the general performance of the FIKS to DMA-train like data.

183   **3.1   DMA-train**

184   The DMA-train is an electrical mobility spectrometer, specifically designed to measure sub-10 nm size-distributions

185   (Stolzenburg et al., 2017). Six identical DMAs are applied in parallel i.e. they sample through the same inlet. They are

186   set to six distinct but fixed voltages and hence classified sizes. The charging state of the aerosol is pre-conditioned in two

187   TSI Inc. Advanced Aerosol Neutralizers (Model 3088), each supplying three DMAs at 5.5 litre per minute (lpm) total

188   flow. We use the Wiedensohler approximation (Wiedensohler, 1988) to describe the steady-state charge distribution at

189   the DMA inlets. Kallinger and Szymanski (2015) showed that for the used neutralizers the steady-state charge distribution

190   is still achieved for flow rates up to 5 lpm. After size classification, the aerosol is detected in condensation particle

191   counters. Four channels are equipped with TSI Inc. Model 3776 ultrafine CPCs for detection of aerosols down to 2.5 nm.

192   They were operated at reduced temperature settings in order to increase the detection efficiency of the smallest particles,

193   achieving a 50% detection efficiency for particles as small as 2 nm (Wlasits et al., 2020). Two channels of the DMA-train

194   were operated with particle counters specifically designed for sub-2 nm particle detection using diethylene glycol (DEG),

195   an Airmodus Ltd. particle size magnifier (Model A10, PSM) and a TSI Inc. nano-Enhancer (Model 3777). Both are used

196   as boosters to activate the particles, which are subsequently detected by either an Airmodus Ltd. CPC (Model A20, for

197   the PSM) or a TSI Inc. CPC (Model 3772, for the nano-Enhancer). Both channels have a higher aerosol flow rate of 2.5

198   lpm resulting in a broader transfer function and higher transmission at the DMA compared to the 1.5 lpm sample flow in

199   the other four channels. The sheath flow at the DMAs is kept constant at 15 lpm for all six channels.

200   The constant sampling at fixed sizes allows for either a higher time-resolution at large aerosol number concentrations or

201   a higher sensitivity towards low number concentrations due to longer signal averaging times compared to a scanning or

202   stepping differential mobility spectrometer. To increase the number of measured particle sizes, one DMA is still operated

203   in an alternating mode, switching between 6.2 and 8 nm every ten seconds. The other DMAs are set to classify particles

204   of 4.3, 3.2, 2.55, 2.2 and 1.8 nm. The instrument kernels are obtained from calibration experiments, where we use the

205   DMA transfer function and sampling loss characterization from Stolzenburg et al. (2017), the CPC activation efficiencies

206   from Wlasits et al. (2020) and the charging efficiency was tested to follow the Wiedensohler approximation in Tauber et

207   al. (2020). The kernel functions for all seven classified sizes are shown in Fig. 1 for an instrument averaging time of 120

208   seconds, sulphuric acid-like test particles (using the Ammonium Sulfate detection efficiencies from Wlasits et al. (2020))

209   and including the detector flow rates of each condensation particle counter. Therefore, the kernels can be used to convert

210   raw particle counts at the detecting CPCs into a particle size-distribution (within an inverse problem) and vice-versa. Note

211   that for different chemical composition of the input particles, the CPC response might be different. Therefore, the kernels

212   used for analysing experiments where particles were formed from oxidized organics (Kirkby et al., 2016) or from iodic

213   acid (He et al., 2021) are different and approximated by the calibration curves for oxidized beta-caryophyllene and sodium

214   chloride from Wlasits et al. (2020).

215
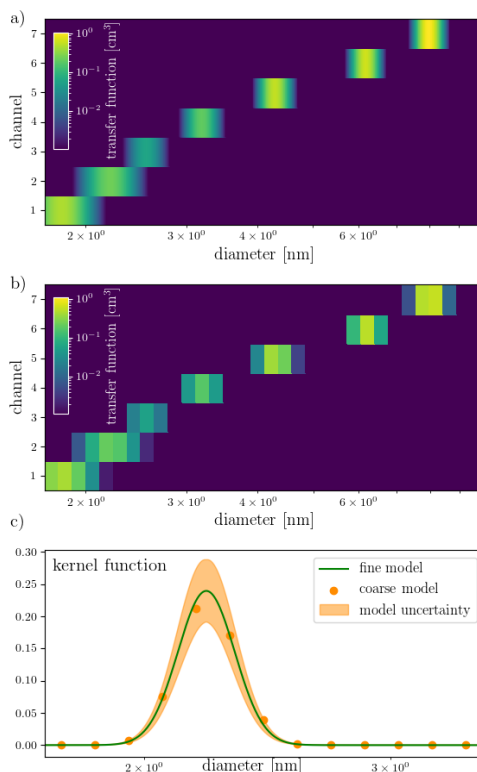
Figure 1: Kernel functions of the DMA-train when classifying sulphuric acid particles at a signal averaging time of 120 seconds. (a) shows the continuous form of the transfer function (color code) of the seven DMA-train channels (y-axis), inferred from instrument calibrations (Stolzenburg et al., 2017). (b) shows the discretization into 32 size bins from 1.7 to 10 nm used in the Kalman smoother (c) shows the comparison between continuous form and used discretization for channel 2 with centroid diameter at 2.2 nm, together with the model uncertainty, which is used for the error estimate (see Table S1 in the Supplement).

221   **3.2   CLOUD**

222   We use experimental data from the DMA-train measuring new particle formation in nucleation experiments at the CERN

223   CLOUD chamber. The 26.1 m^3 stainless-steel chamber provides a high-purity, temperature-controlled environment in

224   order to perform experiments under atmospherically relevant conditions, where trace gases can be added precisely at pptv

225   (parts per trillion by volume) level and sunlight can be simulated by UV-illumination of the chamber. We use three

226 different sets of experiments, of varying chemical composition, in order to demonstrate the performance of the FIKS in

227 reconstructing formation and growth rates. See also Kirkby et al. (2011) and Duplissy et al. (2016).

228 First, a nucleation experiment using sulphuric acid and ammonia was performed at 5℃ by adding SO_2 and O_3 to the

229 chamber and through the photo-dissociation of ozone, the formation of OH radicals and sulphuric acid was induced which

230 resulted in strong new particle formation (Stolzenburg et al., 2020). Second, we performed nucleation and growth

231 experiments at 5℃ using oxidized organics from dark (i.e. no UV-illumination) ozonolysis of alpha-pinene (Kirkby et al.,

232 2016; Stolzenburg et al., 2018). Both experiments resulted in moderate new particle formation rate and thus, in the Kalman

233 smoother, we used DMA-train data that was averaged over 120 seconds time intervals. Third, we studied nucleation from

234 iodine oxides at 10℃ (He et al., 2021), which resulted in high particle formation rates and fast growth. For the third

235 experiment, we reduced the DMA-train averaging time down to 20 seconds, while keeping high counting statistics over

236 the averaging interval.

237 3.3 PSM derived formation rates

238 Particle formation rates (J_{dp}) are calculated from the time derivative of the total particle number concentration larger than

239 1.7 nm following the method introduced in Dada et al. (2020). The particle number size distribution is measured with the

240 particle size magnifier (PSM) coupled with a condensation particle counter (1.5 – 2.5 nm), a TSI nano-SMPS (3 – 65 nm)

241 and home-built long-SMPS (10 – 800 nm). The formation rates are corrected for the size dependent wall and coagulation

242 losses. Additionally, since the chamber is operated in continuous mode, the particle concentrations are corrected for

243 dilution losses. For more information on the PSM derived formation rates, see Dada et al. (2020). The uncertainty on

244 $J_{1.7}$ was assumed to be 30% for the CLOUD chamber calculated using propagation of error in the concentration

245 measurement, dilution, coagulation and wall losses as well as the error on the time-derivative of the total particle

246 concentration.

247 3.4 Growth rates using INSIDE

248 In order to compare the particle growth rates derived by Kalman smoothing, we use the size- and time-dependent growth

249 rate analysis tool INSIDE (Pichelstorfer et al., 2018). It uses input particle size-distributions at time t_1 in order to simulate

250 the known aerosol dynamics (coagulation, wall losses and dilution) until a time t_2 (typically separated by one

251 measurement cycle of an instrument, i.e. the 120 seconds averaging time mentioned above). At t_2, the simulated aerosol

252 size-distribution is compared to the measured size-distribution and by evaluating the general dynamics equation above a

253 certain diameter d_{eval} the growth term $\left.\dfrac{\mathrm{d}d_p}{\mathrm{d}t}\right|_{d_{\mathrm{eval}}} = \dfrac{\left.\frac{\mathrm{d}N_\infty}{\mathrm{d}t}\right|_{d_{\mathrm{eval}}}^{\infty} - \left.\frac{\mathrm{d}N_\infty^{sim}}{\mathrm{d}t}\right|_{d_{\mathrm{eval}}}^{\infty}}{\left.n(d_p,t)\right|_{d_{\mathrm{eval}}}}$ can be computed. Evaluating this equation for

254 several evaluation diameters d_{eval} and at all measurement times t_i, this results in time- and size-resolved growth rates

255 from a size-distribution measurement, which is distinct from most others, integrative growth rate analysis approaches

256 (Dada et al., 2020). However, compared to the Kalman smoothing, each time step is analysed individually and the analysis

257 framework relies on already inverted size distributions, where a point-by-point inversion procedure is used for the DMA-

258 train data of this work (Stolzenburg and McMurry, 2008). Moreover, the INSIDE method does not provide an uncertainty

259 estimate on the growth rate calculation and hence a comparison with other growth rate calculations is beneficial to verify

260 the results.

4 Results: Simulation and Experimental

4.1 Numerical simulation test

First, we modelled the DMA-train instrument numerically and simulated a data set representing a typical nucleation experiment performed in an atmospheric simulation chamber like CLOUD and applied the FIKS to this synthetic dataset. We used the same framework as in Ozon et al. (2020) to simulate a nucleation experiment with formation rate at 1 nm $J_{1.0} = 5.25$ cm^{-3} s^{-1}, and size-independent growth rate $GR = 2.5$ nm h^{-1} and the loss rates equal to the CERN CLOUD experiment (Stolzenburg et al., 2020). The evolution of the simulated size-distribution is shown in Fig. 2a. The measurement data y^k are then simulated using the kernel functions from Fig. 1a and altered with a Poisson-distributed random counting error. The FIKS is then applied to the measurement data with the input parameters given in Table S1 in the Supplement.

Figure 2 also shows the Kalman smoother estimates for the size-distribution, growth rate and formation rate at 1.7 nm. The reconstructed size-distribution (Fig. 2b) is very similar to the true size-distribution (Fig. 2a), especially taking into account the sparser discretization of the former. Also the estimated growth and nucleation rates agree well with true values of the respective process rates specified in the simulation. Moreover, the uncertainty estimates are feasible: For both quantities, the true values are within the uncertainty limits given by FIKS. The reconstructed size-distribution and especially, growth rate (Fig. 2 b and c, respectively) show some temporal oscillations, which are related to periods for the particle population to grow from the size range visible for one DMA-train channel to the next one. That is, the oscillation is a result of an insufficient coverage of the size-range by the DMA-train kernels and is discussed in more detail in Section 4.5. Nevertheless, the overall good retrieval of the simulated size distribution and process rates demonstrates that Kalman smoothing approach is well suited for analysing DMA-train data from chamber nucleation experiments.
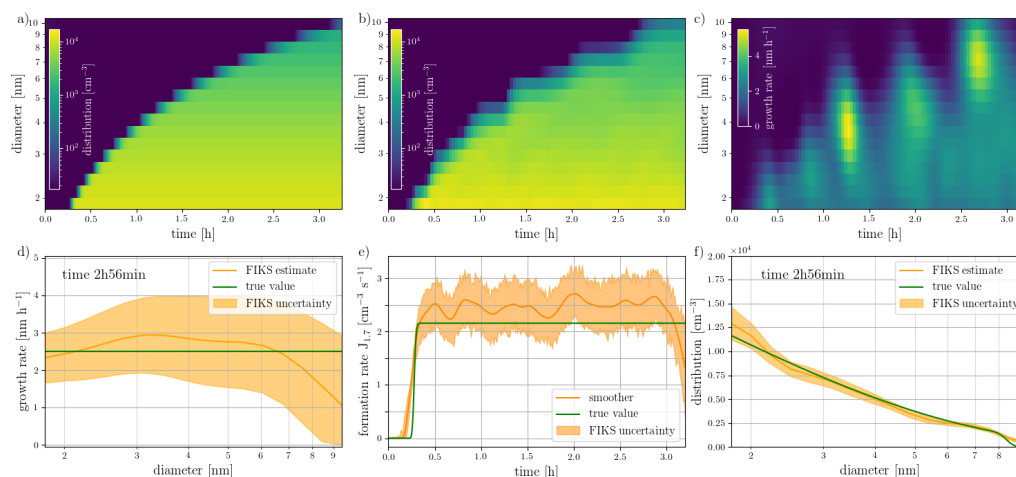

Figure 2: Results of the simulated chamber nucleation experiment: (a) The simulated, temporally evolving size distribution of aerosols. (b) The FIKS estimate for the size distribution. This estimate was computed based on the numerically simulated DMA-train data corresponding to the synthetic size distribution shown in (a). (c) The FIKS estimate for the growth rate of particles. (d) The growth rate corresponding to a single instant of time (2h 56min); here, the FIKS estimate and the associated uncertainty limits are plotted together with the true growth rate. (e) The FIKS estimate for the formation rate at 1.7 nm and its uncertainty, and the true formation rate. (f) FIKS estimate, its uncertainty and the true value of the particle size distribution corresponding to a single instant of time (2h 56min). In subfigures d-f, the orange lines represent the FIKS estimates (posterior expectations) and the orange shaded areas illustrate the uncertainties of the associated variables (more specifically, their approximate posterior standard deviation limits). The true values of the quantities are plotted in green.

4.2 Sulphuric Acid-Ammonia experiment

We applied the FIKS to experimental data from a sulphuric acid-ammonia nucleation and growth experiment performed at 5℃ at the CERN CLOUD chamber. The raw data measured with the DMA-train were averaged in 120-second time intervals in order to increase the counting statistics per channel and then used as input for BAYROSOL. The details of parameter choices in FIKS are given again in Table S1 in the Supplement. The results of applying the Kalman smoothing to this experimental data are shown in Fig. 3.
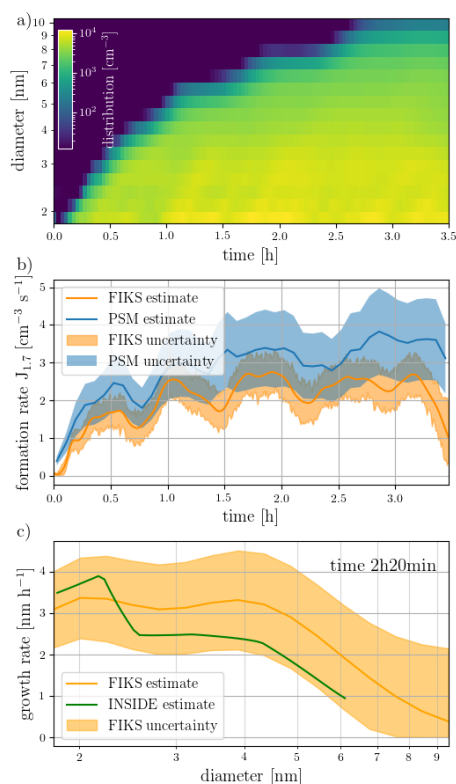
Figure 3: Results of an experiment performed at the CERN CLOUD chamber: The DMA-train data was acquired during sulphuric acid-ammonia nucleation and growth processes. Experimental conditions: 5℃, 60% RH, 5 ppb SO_2, 120 ppb O_3 and 40 ppt NH_3. (a) The FIKS estimate for the size distribution. (b) The evolution of the formation rate during the experiment. The orange line and shaded area represent the FIKS estimate and its uncertainty, respectively, while the solid blue line and blue area show the nucleation rate estimate and the associated 30% uncertainty based on a different set of instruments (particle size magnifier, PSM) and the standard approach for inferring nucleation rates at 1.7 nm (Dada et al., 2020). (c) The growth rate corresponding to time 2h19 min after the start of the experiment. The FIKS estimate and the associated uncertainty are marked with orange line and shaded area, respectively. The green line represents the growth rate estimate, which is obtained from DMA-train data by traditional inversion (INSIDE method).

The size- and time-dependence of the FIKS estimate for the true size-distribution (Fig. 3a) is very smooth, and it is also able to bridge the information gaps between the largest size-distribution channels. This is a significant improvement from the traditional point-by-point inversion, where the data of each DMA-train channel is inverted independently: When point-by-point inversion was applied to the same dataset, those information gaps caused severe reconstruction errors (discontinuities) in the size-distribution, see (Stolzenburg et al., 2020). The size-distribution shows also small temporal fluctuations. The fluctuations are even more clearly visible in the reconstructed evolution of the formation rate (Fig. 3b). Remarkably, the same fluctuations are also recovered when the formation rate is inferred from the PSM and nano-SMPS,

313   i.e. an entirely different set of instrumentation and different type of data-analysis. This result strongly suggests that the

314   fluctuation of the particle formation truly occurs physically in the experiment and is not a reconstruction error caused by

315   instrument noise or a bias caused by the inversion method. The absolute values of the two independent formation rate

316   estimates agree upon a factor of 1.5. Furthermore, large portions of the uncertainty intervals of these two estimates overlap

317   with each other, which is another indicator of the feasibility of FIKS to analysing DMA-train data. In addition, also the

318   inferred growth rates agree within the systematic uncertainties for both approaches (Fig. 3c for one time instant). It is

319   worth noting, however, that both growth rate estimates rely on data from the same instrument and are hence more

320   interdependent than the formation rate estimates. Nevertheless, the good agreement between them corroborates the

321   feasibility of Kalman smoothing to reconstructing nanoparticle growth rates from experimental data.

4.3   Alpha-pinene ozonolysis experiment

323   Third, we applied the FIKS to experimental data obtained by the DMA-train from an alpha-pinene ozonolysis experiment.

324   Besides the different chemical composition of the growing particles (resulting in different assumptions on the DMA-train

325   transfer functions) in comparison to the experimental results used in section 4.2, this experiment is characterized by a

326   different size-dependency of the growth rate, due to the increased condensation of low- and semi-volatile organics with

327   increasing particle size (Simon et al., 2020; Stolzenburg et al., 2018; Tröstl et al., 2016). The formation rate, however,

328   remains rather similar to the sulphuric acid-ammonia experiment under these specific experimental conditions, but the

329   slower initial growth rates result in generally lower produced particle concentrations. The results of applying FIKS to the

330   data from this experiment are shown in Fig. 4. Again, the size-distribution given by FIKS is much smoother than that

331   obtained with a standard inversion procedure (see Heinritzi et al. (2020) for the same dataset inverted by the standard

332   approach).

333   Because in alpha-pinene ozonolysis experiment the nucleation and growth rates were known to be similar to those in the

334   sulphuric acid-ammonia experiment, the parameters of their evolution models were selected as in Section 4.2 (Table S1

335   in the Supplement). The formation rate is again slightly lower than the one obtained from the PSM. Considering the fact

336   that inter-instrument deviations in sub-10 nm size-distribution measurements can be as large as one order of magnitude

337   (Kangasluoma et al., 2020), the achieved agreement is remarkable, especially as some fluctuations within the chamber

338   can again be reconstructed in both approaches. The retrieved growth rates from the FIKS estimate and the INSIDE method

339   agree remarkably well and both show the increasing growth rates with increasing particle size up to 4.3 nm, an indication

340   for a strong Kelvin-effect in organic condensation (Stolzenburg et al., 2018; Tröstl et al., 2016). The decreasing Kalman

341   smoother estimate above 4.3 nm is related to the fact that the FIKS searches a smooth estimate of the growth rate (Eq.

342   (6)), but at that point (2h30min after experiment start), practically no information from the size-distribution above 4.3 nm

343   is available, resulting in a slow decrease towards zero. This is due to the strong smoothness a priori used in the FIKS

344   algorithm (Table S1 in the Supplement). The INSIDE method does not report growth rates from regions with no

345   information (Pichelstorfer et al., 2018) from the size-distribution and hence the estimate stops at 4.3 nm.
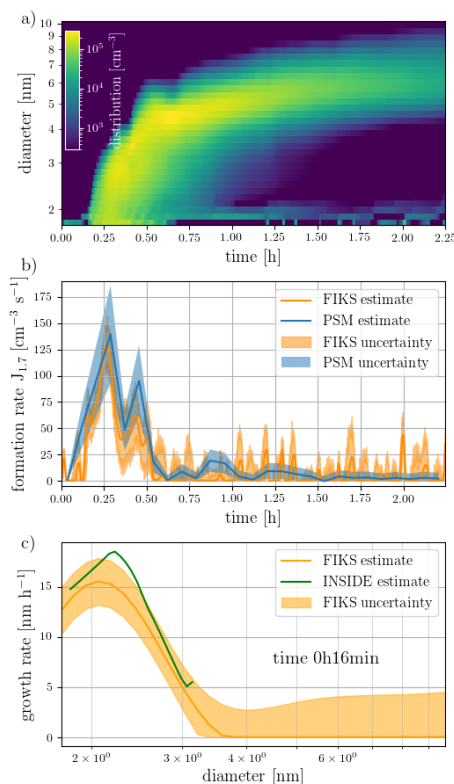
Atmospheric
Chemistry
and Physics
Discussions
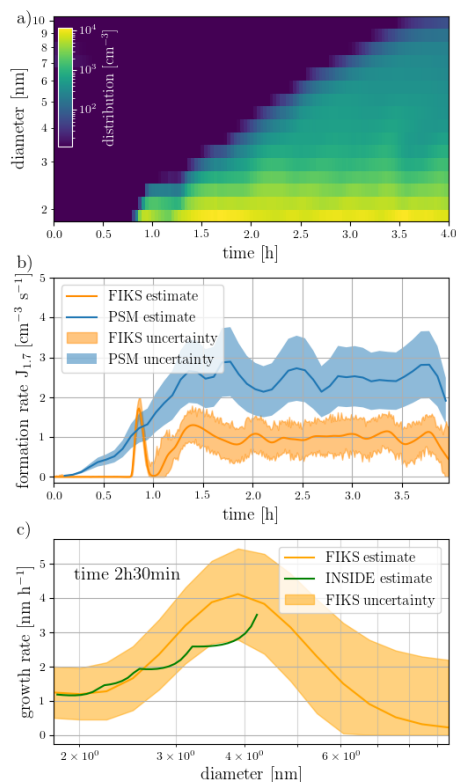
Figure 4: Results of an experiment performed at the CERN CLOUD chamber: The DMA-train data was acquired during an alpha-pinene ozonolysis. Experimental conditions: Experimental conditions: 5℃, 40% RH, 300 ppt alpha-pinene, 40 ppb O_3. (a) The FIKS estimate for the size distribution. (b) The evolution of the formation rate during the experiment. The orange line and shaded area represent the FIKS estimate and its uncertainty, respectively, while the solid blue line and blue area show the nucleation rate estimate and the associated 30% uncertainty based on a different set of instruments (particle size magnifier, PSM) and the standard approach for inferring nucleation rates at 1.7 nm (Dada et al., 2020). (c) The growth rate corresponding to time 2h30 min after the start of the experiment. The FIKS estimate and the associated uncertainty are marked with orange line and shaded area, respectively. The green line represents the growth rate estimate, which is obtained from DMA-train data by traditional inversion (INSIDE method).

4.4   Iodic Acid experiment

Finally, we analysed a more dynamic experiment of nucleation and growth from iodic acid (He et al., 2020, 2021). The experiment is characterized by extremely high nucleation rates, which are two orders of magnitude higher than in the sulphuric acid-ammonia and alpha-pinene ozonolysis experiments. However, the growth rate is only half an order of magnitude higher compared to the other two example cases. Figure 5 shows that, in spite of the highly dynamic experiment, the formation rate recovered by Kalman smoothing agrees with the estimate obtained from the PSM (Fig. 5b). The usage of the DMA-train data with a time resolution of 20 seconds allows for the precise recovery of the spike in formation rate in the beginning of the experiment. This causes the build-up of a high condensation sink and vapour/cluster depletion almost shutting off any further nucleation during the continuation of the experiment. The four-minute time resolution of the data for the calculation of the nucleation rate from the PSM is limited in that respect. The reconstructed growth rates (Fig. 5c) show again agreement between the FIKS estimate and the INSIDE method, indicating a clear decreasing trend with size, which is expected for condensation at the kinetic limit if the vapour molecular size is taken into account (He et al., 2021; Lehtinen and Kulmala, 2003; Nieminen et al., 2010; Stolzenburg et al., 2020). The lower

368   values towards 1.8 nm could be caused by a biased estimate of the PSM detection efficiency, because neither a calibration

369   for iodic acid clusters nor for sodium chloride particles (which was used for the other detectors in the DMA-train) was

370   available. The instabilities in the size-distribution at the smallest sizes and fluctuations of the formation rate are expected

371   considering the highly dynamic process of this experiment Overall, the good agreement for the inferred process

372   parameters of the aerosol general dynamics equation, i.e. the formation and growth rates, is still remarkable. However,

373   the reconstructed size-distribution from the FIKS estimate shows some discontinuities, especially during the growth above

374   3 nm. This is because the available instrument information from the DMA-train starts to get very sparse in that size range

375   given the dynamic processes involved in the iodic acid nucleation and growth. More available size channels (hence more

376   DMAs in the case of the DMA-train) would help to resolve such discontinuities. We will therefore provide an instrument

377   design recommendation based on simulated data in the next section.

378

Figure 5: Results of an experiment performed at the CERN CLOUD chamber: The DMA-train data was acquired during iodic acid
nucleation and growth processes. Experimental conditions: Experimental conditions: 10℃, 80% RH, 100 ppt I_2, 40 ppb O_3. (a) The
FIKS estimate for the size distribution. (b) The evolution of the formation rate during the experiment. The orange line and shaded area
represent the FIKS estimate and its uncertainty, respectively, while the solid blue line and blue area show the nucleation rate estimate
and the associated 30% uncertainty based on a different set of instruments (particle size magnifier, PSM) and the standard approach
for inferring nucleation rates at 1.7 nm (Dada et al., 2020). (c) The growth rate corresponding to time 0h16min min after the start of
the experiment. The FIKS estimate and the associated uncertainty are marked with orange line and shaded area, respectively. The green
line represents the growth rate estimate, which is obtained from DMA-train data by traditional inversion (INSIDE method).

387   **4.5   Instrument design recommendation from a signal processing point of view**

388   The size range covered by the seven DMA-train channels was chosen semi-arbitrarily based on some external constraints:

389   the lowest measured centroid diameter was supposed to be as close as possible to 1.7 nm where the formation rate is

390 typically measured for experiments performed at the CLOUD chamber. In order to cover the sub-10 nm range the largest

391 channels was set to 8 nm. The other channel diameters were chosen to yield sufficient coverage of the sub-3 nm range.

392 The width of the transfer functions was fixed by the detector sample flow rates and the 15 lpm critical orifices provided

393 by Grimm Aerosol for the DMA sheath air supply (also the standard flow rate used by the manufacturer for this type of

394 DMA). However, the chosen centroid diameters (and hence fixed voltages at the DMAs) and selected sheath flow rates

395 could easily be altered.

396 In order to study numerically the effect of choice for the DMA-train channels, we constructed a model corresponding to

397 a channel choice different from that in the previous sections: The kernel for the DMA-train with seven channels having

398 centroid diameters of 1.8, 2.2, 2.8, 3.6, 4.6, 6.1 and 8.0 nm is illustrated in Fig. 6a. Moreover, channels 3 to 7 have been

399 altered to use a 2.5 lpm sample flow rate (could be achieved by a make-up flow at each CPC) and a reduced sheath flow

400 rate of 10 lpm, only providing a resolution of theoretical non-diffusive resolution of ~4, which is significantly lower.

401 However, this permits covering the entire size-range between 1.8 and 8 nm by overlapping channels. We revisited the

402 numerical simulation described in Section 4.1 using DMA-train model corresponding to this configuration. The resulting

403 size-distribution given by FIKS is shown in Fig. 6b. Comparison between the two reconstructions in Fig. 2b and Fig. 6b

404 reveals that the new choice of DMA-channels stabilizes the size-distribution estimate significantly. While in Fig. 2b, the

405 size distribution evolves in step-wise manner when the growing particle mode reaches larger size-channels, the size

406 distribution in Fig. 6b is very smooth, also temporally. The latter estimate also resembles the true (simulated) size-

407 distribution (Fig. 2a) more than the former one.

408 The result of this additional numerical study thus demonstrates that in the chosen conditions of the simulation, the

409 reconstruction quality improves when the resolution of individual channels is lowered. This seemingly counterintuitive

410 effect stems from the fact that FIKS estimates do not rely only on the measurements, but are also advised by the GDE

411 model, which makes the problem of optimizing the measurement design a somewhat cumbersome task. A rigorous

412 investigation of the optimal experimental design is out of the scope of this paper, but the above observation is worth

413 noticing -- especially because a lot of recent experimental effort in the sub-10 nm range has been devoted to improving

414 the instrument resolution (Kangasluoma et al., 2020). While on the individual channel level this might reduce systematic

415 uncertainties, as discussed in Kangasluoma et al. (2020), signal processing rather requires a broad coverage of the size

416 distribution than high resolution. However, the ideal instrument would combine both, full coverage of the size distribution

417 but achieved with more, high-resolution channels. For the DMA-train principle, this would require new ideas in

418 instrument design in order to incorporate more DMAs without the instrument becoming impractically bulky.

419
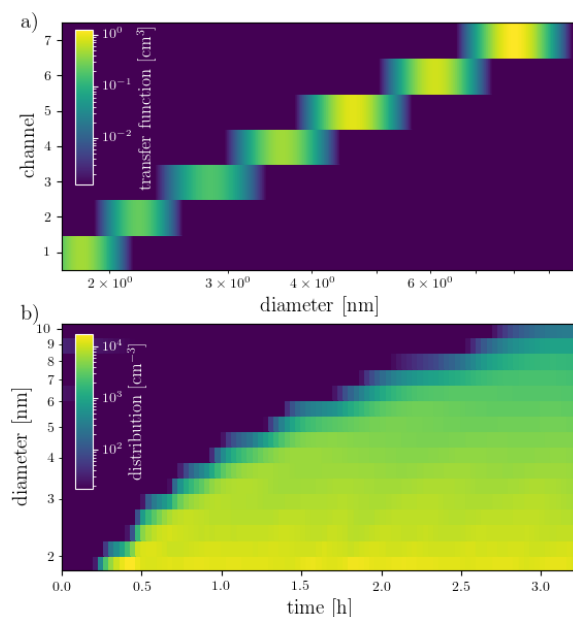
Figure 6: Adjusted DMA-train kernel for better signal processing (a), which could be achieved by choosing suitable centroid voltages and altering the resolution of the DMAs through sheath-flow and sample-flow adjustments. (b) shows the reconstructed simulated size-distribution of Fig. 2 using the adjusted kernel.

5   Conclusion

A recently developed methodology (BAYROSOL) applying the Fixed Interval Kalman Smoother (FIKS) to a finite difference solution to the aerosol GDE was used to analyze DMA-train measurements of aerosol dynamics at the CLOUD chamber facility at CERN. The overall aim of this methodology is to estimate unknown aerosol microphysical process rates as well as their uncertainties from size-distribution evolution measurements. In a previous paper, the methodology was shown to be able to predict new particle formation, growth and loss rates from synthetic computer-generated aerosol size distribution evolution data, while here the method has been applied to real experimental data for the first time. Four experimental cases with particle formation and growth were tested: 1) a computer-generated synthetic case, 2) sulphuric acid-ammonia, 3) alpha-pinene ozonolysis, and 4) iodic acid.

The DMA-train was selected for two main reasons: first, the instrument kernel functions are well characterized giving rise to reliable estimation of the instrument uncertainties and second, new particle formation rates have not been estimated directly from DMA-train measurements before. In addition, as the current version of the DMA-train is designed in such a way that the individual DMAs have a rather narrow collection kernels for the channels, with significant gaps between some of the channels, the FIKS can reconstruct the size distributions from the measured signals in such a way that the distributions are rather smooth and consistent with the GDE.

We compared the growth rates, which with BAYROSOL can be estimated as functions of both size and time, with those obtained by INSIDE, a method applied earlier to CLOUD data, and the agreement was remarkably good for all studied cases. INSIDE is also based on matching the GDE solution to measured size distribution dynamics, however without the capability of estimating uncertainties of the estimations. The FIKS-based estimates for the particle formation rates were compared with those estimated from data obtained by a separate instrument, the Particle Size Magnifier (PSM), based on

443 the rate of change of the total number concentration measured by the instrument corrected by coagulation and wall-losses.

444 Again, the agreement was very good, especially considering the fact that instrument uncertainties are large at the very

445 lowest end of the measured size spectrum. For the iodic-acid case, the FIKS estimate of the formation rate was even able

446 to capture rapidly changing dynamics of the experiment. It was remarkable for all cases that some fluctuations in the

447 formation rates were recovered by both methods independently, indicating that these are physical variations during the

448 experiment

449 Finally, we utilized the FIKS from an instrument development point of view. Typically, an as-high-as-possible resolution

450 for the different measurement channels has been the aim when measuring nanometer-sized particles. This aim, however,

451 gives rise to gaps in the measured size range, as is the case in the DMA-train studied. Thus we studied whether a better

452 coverage of the size spectrum, but lower resolution of the individual channels would be advantageous for size distribution

453 estimation.

454 Summarizing, we believe that Bayesian state estimation methods such as FIKS can be very useful in the field of aerosol

455 science in many aspects. As mentioned above, they can be used to fill gaps in measurements in such a way that not only

456 the obtained size distributions but also unknown process rates are consistent with theory describing aerosol size

457 distribution dynamics. In addition, the methodology provides estimations of uncertainties both for size distributions as

458 well as process rates based on uncertainty estimations in the measurements and the used models, which is unfortunately

459 not common when reporting results of aerosol measurements. Finally, it is conceivable that the methodology presented

460 here will be superior to several previous approaches when combining measurement data obtained with several different

461 instruments that operate at different size ranges. This will be a topic of our forthcoming studies.

462 **Data availability**

463 The version of the implementation of the estimation method (BAYROSOL1.1)[https://doi.org/10.5281/zenodo.4450492]

464 is available under the MIT Expat License; it is the version used to generate the results discussed in this paper. The package

465 also contains the code used to obtain the results discussed in Ozon et al. 2020. It is possible to generate the simulated data

466 described in section 4.1. The experimental data (DMA-train kernels) and raw data, are also included in the repository.

467 **Competing interest**

468 The authors declare no competing interests.

469 **Acknowledgements**

Author contributions

MO, DS, LD analysed the experimental data, MO developed the software, all authors were involved in the scientific discussion and in the writing of the manuscript.

References

Albrecht, B. A.: Aerosols, Cloud Microphysics, and Fractional Cloudiness, Science, 245(4923), 1227–1230, doi:10.1126/science.245.4923.1227, 1989.

Appel, B. R., Tokiwa, Y., Hsu, J., Kothny, E. L. and Hahn, E.: Visibility as related to atmospheric aerosol constituents, Atmos. Environ., 19(9), 1525–1534, doi:https://doi.org/10.1016/0004-6981(85)90290-2, 1985.

Chambolle, A. and Pock, T.: A First-Order Primal-Dual Algorithm for Convex Problems with Applications to Imaging, J. Math. Imaging Vis., 40(1), 120–145, doi:10.1007/s10851-010-0251-1, 2011.

Dada, L., Lehtipalo, K., Kontkanen, J., Nieminen, T., Baalbaki, R., Ahonen, L., Duplissy, J., Yan, C., Chu, B., Petäjä, T., Lehtinen, K., Kerminen, V.-M., Kulmala, M. and Kangasluoma, J.: Formation and growth of sub-3-nm aerosol particles in experimental chambers, Nat. Protoc., doi:10.1038/s41596-019-0274-z, 2020.

Daellenbach, K. R., Uzu, G., Jiang, J., Cassagnes, L.-E., Leni, Z., Vlachou, A., Stefenelli, G., Canonaco, F., Weber, S., Segers, A., Kuenen, J. J. P., Schaap, M., Favez, O., Albinet, A., Aksoyoglu, S., Dommen, J., Baltensperger, U., Geiser, M., El Haddad, I., Jaffrezo, J.-L. and Prévôt, A. S. H.: Sources of particulate-matter air pollution and its oxidative potential in Europe, Nature, 587(7834), 414–419, doi:10.1038/s41586-020-2902-8, 2020.

Duplissy, J., Merikanto, J., Franchin, A., Tsagkogeorgas, G., Kangasluoma, J., Wimmer, D., Vuollekoski, H., Schobesberger, S., Lehtipalo, K., Flagan, R. C., Brus, D., Donahue, N. M., Vehkamäki, H., Almeida, J., Amorim, A., Barmet, P., Bianchi, F., Breitenlechner, M., Dunne, E. M., Guida, R., Henschel, H., Junninen, H., Kirkby, J., Kürten, A., Kupc, A., Määttänen, A., Makhmutov, V., Mathot, S., Nieminen, T., Onnela, A., Praplan, A. P., Riccobono, F., Rondo, L., Steiner, G., Tome, A., Walther, H., Baltensperger, U., Carslaw, K. S., Dommen, J., Hansel, A., Petäjä, T., Sipilä, M., Stratmann, F., Vrtala, A., Wagner, P. E., Worsnop, D. R., Curtius, J. and Kulmala, M.: Effect of ions on sulfuric acid-water binary particle formation: 2. Experimental data and comparison with QC-normalized classical nucleation theory, J. Geophys. Res.-Atmos., 121(4), 1752–1775, doi:10.1002/2015JD023539, 2016.

Gelb, A.: Applied optimal estimation, MIT Press, Cambridge, Massachusetts., 1974.

He, X.-C., Iyer, S., Sipilä, M., Ylisirniö, A., Peltola, M., Kontkanen, J., Baalbaki, R., Simon, M., Kürten, A., Tham, Y. J., Pesonen, J., Ahonen, L. R., Amanatidis, S., Amorim, A., Baccarini, A., Beck, L., Bianchi, F., Brilke, S., Chen, D., Chiu, R., Curtius, J., Dada, L., Dias, A., Dommen, J., Donahue, N. M., Duplissy, J., El Haddad, I., Finkenzeller, H., Fischer, L., Heinritzi, M., Hofbauer, V., Kangasluoma, J., Kim, C., Koenig, T. K., Kubečka, J., Kvashnin, A., Lamkaddam, H., Lee, C. P., Leiminger, M., Li, Z., Makhmutov, V., Xiao, M., Marten, R., Nie, W., Onnela, A., Partoll, E., Petäjä, T., Salo, V.-T., Schuchmann, S., Steiner, G., Stolzenburg, D., Stozhkov, Y., Tauber, C., Tomé, A., Väisänen, O., Vazquez-Pufleau, M., Volkamer, R., Wagner, A. C., Wang, M., Wang, Y., Wimmer, D., Winkler, P. M., Worsnop, D. R., Wu, Y., Yan, C., Ye, Q., Lehtinen, K., Nieminen, T., Manninen, H. E., Rissanen, M., Schobesberger, S., Lehtipalo, K., Baltensperger, U., Hansel, A., Kerminen, V.-M., Flagan, R. C., Kirkby, J., Kurtén, T. and Kulmala, M.: Determination of the collision rate coefficient between charged iodic acid clusters and iodic acid using the appearance time method, Aerosol Sci. Tech., 1–12, doi:10.1080/02786826.2020.1839013, 2020.

He, X.-C., Tham, Y. J., Dada, L., Wang, M., Finkenzeller, H., Stolzenburg, D., Iyer, S., Simon, M., Kürten, A., Shen, J.,

514   Rörup, B., Rissanen, M., Schobesberger, S., Baalbaki, R., Wang, D. S., Koenig, T. K., Jokinen, T., Sarnela, N., Beck, L.,

515   Almeida, J., Amanatidis, S., Amorim, A., Ataei, F., Baccarini, A., Bertozzi, B., Bianchi, F., Brilke, S., Caudillo, L., Chen,

516   D., Chiu, R., Chu, B., Dias, A., Ding, A., Dommen, J., Duplissy, J., El-Haddad, I., Gonzalez Carracedo, L., Granzin, M.,

517   Hansel, A., Heinritzi, M., Hofbauer, V., Junninen, H., Kangasluoma, J., Kemppainen, D., Kim, C., Kong, W., Krechmer,

518   J. E., Kvashnin, A., Laitinen, T., Lamkaddam, H., Lee, C. P., Lehtipalo, K., Leiminger, M., Li, Z., Makhmutov, V.,

519   Manninen, H. E., Marie, G., Marten, R., Mathot, S., Mauldin, R. L., Mentler, B., Möhler, O., Müller, T., Nie, W., Onnela,

520   A., Petäjä, T., Pfeifer, J., Philippov, M., Ranjithkumar, A., Saiz-Lopez, A., Salma, I., Scholz, W., Schuchmann, S.,

521   Schulze, B., Steiner, G., Stozhkov, Y., Tauber, C., Tomé, A., Thakur, R. C., Väisänen, O., Vazquez-Pufleau, M., Wagner,

522   A. C., Wang, Y., Weber, S. K., Winkler, P. M., Wu, Y., Xiao, M., Yan, C., Ye, Q., Ylisirniö, A., Zauner-Wieczorek, M.,

523   Zha, Q., Zhou, P., Flagan, R. C., Curtius, J., Baltensperger, U., Kulmala, M., Kerminen, V.-M., Kurten, T., et al.: Role of

524   iodine oxoacids in atmospheric aerosol nucleation, Science, 371(6529), 589–595, doi:10.1126/science.abe0298, 2021.

525   Heinritzi, M., Dada, L., Simon, M., Stolzenburg, D., Wagner, A. C., Fischer, L., Ahonen, L. R., Amanatidis, S., Baalbaki,

526   R., Baccarini, A., Bauer, P. S., Baumgartner, B., Bianchi, F., Brilke, S., Chen, D., Chiu, R., Dias, A., Dommen, J.,

527   Duplissy, J., Finkenzeller, H., Frege, C., Fuchs, C., Garmash, O., Gordon, H., Granzin, M., El Haddad, I., He, X., Helm,

528   J., Hofbauer, V., Hoyle, C. R., Kangasluoma, J., Keber, T., Kim, C., Kürten, A., Lamkaddam, H., Laurila, T. M.,

529   Lampilahti, J., Lee, C. P., Lehtipalo, K., Leiminger, M., Mai, H., Makhmutov, V., Manninen, H. E., Marten, R., Mathot,

530   S., Mauldin, R. L., Mentler, B., Molteni, U., Müller, T., Nie, W., Nieminen, T., Onnela, A., Partoll, E., Passananti, M.,

531   Petäjä, T., Pfeifer, J., Pospisilova, V., Quéléver, L. L. J., Rissanen, M. P., Rose, C., Schobesberger, S., Scholz, W.,

532   Scholze, K., Sipilä, M., Steiner, G., Stozhkov, Y., Tauber, C., Tham, Y. J., Vazquez-Pufleau, M., Virtanen, A., Vogel, A.

533   L., Volkamer, R., Wagner, R., Wang, M., Weitz, L., Wimmer, D., Xiao, M., Yan, C., Ye, P., Zha, Q., Zhou, X., Amorim,

534   A., Baltensperger, U., Hansel, A., Kulmala, M., Tomé, A., Winkler, P. M., Worsnop, D. R., Donahue, N. M., Kirkby, J.

535   and Curtius, J.: Molecular understanding of the suppression of new-particle formation by isoprene, Atmos. Chem. Phys.,

536   20(20), 11809–11821, doi:10.5194/acp-20-11809-2020, 2020.

537   Henze, D. K., Seinfeld, J. H., Liao, W., Sandu, A. and Carmichael, G. R.: Inverse modeling of aerosol dynamics:

538   Condensational growth, J. Geophys. Res.-Atmos., 109(D14), doi:https://doi.org/10.1029/2004JD004593, 2004.

539   Kaipio, J. and Somersalo, E.: Statistical and Computational Inverse Problems, Springer-Verlag, New York., 2005.

540   Kallinger, P. and Szymanski, W. W.: Experimental determination of the steady-state charging probabilities and particle

541   size conservation in non-radioactive and radioactive bipolar aerosol chargers in the size range of 5-40 nm, J. Nanopart.

542   Res., 17(4), 171, doi:10.1007/s11051-015-2981-x, 2015.

543   Kandlikar, M. and Ramachandran, G.: Inverse methods for analysing aerosol spectrometer measurements: a critical

544   review, J. Aerosol Sci., 30(4), 413–437, doi:https://doi.org/10.1016/S0021-8502(98)00066-4, 1999.

545   Kangasluoma, J., Cai, R., Jiang, J., Deng, C., Stolzenburg, D., Ahonen, L. R., Chan, T., Fu, Y., Kim, C., Laurila, T. M.,

546   Zhou, Y., Dada, L., Sulo, J., Flagan, R. C., Kulmala, M., Petäjä, T. and Lehtipalo, K.: Overview of measurements and

547   current instrumentation for 1–10 nm aerosol particle number size distributions, J. Aerosol Sci., 105584,

548   doi:https://doi.org/10.1016/j.jaerosci.2020.105584, 2020.

549   Kirkby, J., Curtius, J., Almeida, J., Dunne, E., Duplissy, J., Ehrhart, S., Franchin, A., Gagné, S., Ickes, L., Kürten, A.,

550   Kupc, A., Metzger, A., Riccobono, F., Rondo, L., Schobesberger, S., Tsagkogeorgas, G., Wimmer, D., Amorim, A.,

551   Bianchi, F., Breitenlechner, M., David, A., Dommen, J., Downard, A., Ehn, M., Flagan, R. C., Haider, S., Hansel, A.,

552   Hauser, D., Jud, W., Junninen, H., Kreissl, F., Kvashin, A., Laaksonen, A., Lehtipalo, K., Lima, J., Lovejoy, E. R.,

553   Makhmutov, V., Mathot, S., Mikkilä, J., Minginette, P., Mogo, S., Nieminen, T., Onnela, A., Pereira, P., Petäjä, T.,

554   Schnitzhofer, R., Seinfeld, J. H., Sipilä, M., Stozhkov, Y., Stratmann, F., Tomé, A., Vanhanen, J., Viisanen, Y., Vrtala,

555   A., Wagner, P. E., Walther, H., Weingartner, E., Wex, H., Winkler, P. M., Carslaw, K. S., Worsnop, D. R., Baltensperger,

556   U. and Kulmala, M.: Role of sulphuric acid, ammonia and galactic cosmic rays in atmospheric aerosol nucleation, Nature,

557   476, 429–433, doi:10.1038/nature10343, 2011.

558   Kirkby, J., Duplissy, J., Sengupta, K., Frege, C., Gordon, H., Williamson, C., Heinritzi, M., Simon, M., Yan, C., Almeida,

559   J., Tröstl, J., Nieminen, T., Ortega, I. K., Wagner, R., Adamov, A., Amorim, A., Bernhammer, A.-K., Bianchi, F.,

560   Breitenlechner, M., Brilke, S., Chen, X., Craven, J., Dias, A., Ehrhart, S., Flagan, R. C., Franchin, A., Fuchs, C., Guida,

561   R., Hakala, J., Hoyle, C. R., Jokinen, T., Junninen, H., Kangasluoma, J., Kim, J., Krapf, M., Kürten, A., Laaksonen, A.,

562   Lehtipalo, K., Makhmutov, V., Mathot, S., Molteni, U., Onnela, A., Peräkylä, O., Piel, F., Petäjä, T., Praplan, A. P.,

563   Pringle, K., Rap, A., Richards, N. A. D., Riipinen, I., Rissanen, M. P., Rondo, L., Sarnela, N., Schobesberger, S., Scott,

564   C. E., Seinfeld, J. H., Sipilä, M., Steiner, G., Stozhkov, Y., Stratmann, F., Tomé, A., Virtanen, A., Vogel, A. L., Wagner,

565   A. C., Wagner, P. E., Weingartner, E., Wimmer, D., Winkler, P. M., Ye, P., Zhang, X., Hansel, A., Dommen, J., Donahue,

566   N. M., Worsnop, D. R., Baltensperger, U., Kulmala, M., Carslaw, K. S. and Curtius, J.: Ion-induced nucleation of pure

567   biogenic particles, Nature, 533, 521–526, doi:10.1038/nature17953, 2016.

568   Kuang, C., Chen, M., Zhao, J., Smith, J., McMurry, P. H. and Wang, J.: Size and time-resolved growth rate measurements

569   of 1 to 5 nm freshly formed atmospheric nuclei, Atmos. Chem. Phys., 12(7), 3573–3589, doi:10.5194/acp-12-3573-2012,

570   2012.

571   Kulmala, M., Petäjä, T., Nieminen, T., Sipilä, M., Manninen, H. E., Lehtipalo, K., Dal Maso, M., Aalto, P. P., Junninen,

572   H., Paasonen, P., Riipinen, I., Lehtinen, K. E. J., Laaksonen, A. and Kerminen, V.-M.: Measurement of the nucleation of

573   atmospheric aerosol particles, Nat. Protoc., 7(9), 1651–1667, doi:10.1038/nprot.2012.091, 2012.

574   Kupiainen-Määttä, O.: A Monte Carlo approach for determining cluster evaporation rates from concentration

575   measurements, Atmos. Chem. Phys., 16(22), 14585–14598, doi:10.5194/acp-16-14585-2016, 2016.

576   Kürten, A., Li, C., Bianchi, F., Curtius, J., Dias, A., Donahue, N. M., Duplissy, J., Flagan, R. C., Hakala, J., Jokinen, T.,

577   Kirkby, J., Kulmala, M., Laaksonen, A., Lehtipalo, K., Makhmutov, V., Onnela, A., Rissanen, M. P., Simon, M., Sipilä,

578   M., Stozhkov, Y., Tröstl, J., Ye, P. and McMurry, P. H.: New particle formation in the sulfuric acid--dimethylamine--

579   water system: reevaluation of CLOUD chamber measurements and comparison to an aerosol nucleation and growth

580   model, Atmos. Chem. Phys., 18(2), 845–863, doi:10.5194/acp-18-845-2018, 2018.

581   Lehtinen, K. E. J. and Kulmala, M.: A model for particle formation and growth in the atmosphere with molecular

582   resolution in size, Atmos. Chem. Phys., 3(1), 251–257, doi:10.5194/acp-3-251-2003, 2003.

583   Lehtinen, K. E. J., Rannik, Ü., Petäjä, T., Kulmala, M. and Hari, P.: Nucleation rate and vapor concentration estimations

584   using a least squares aerosol dynamics method, J. Geophys. Res.-Atmos., 109(D21), doi:10.1029/2004JD004893, 2004.

585   McGuffin, D. L., Huang, Y., Flagan, R. C., Petäjä, T., Ydstie, B. E. and Adams, P. J.: Novel estimation of aerosol

586   processes with particle size distribution measurements: a case study with TOMAS algorithm, Geosci. Model Dev.

587   Discuss., 2020, 1–27, doi:10.5194/gmd-2020-281, 2020.

588   Nieminen, T., Lehtinen, K. E. J. and Kulmala, M.: Sub-10 nm particle growth by vapor condensation – effects of vapor

589   molecule size and particle thermal speed, Atmos. Chem. Phys., 10(20), 9773–9779, doi:10.5194/acp-10-9773-2010, 2010.

590   Nieminen, T., Kerminen, V.-M., Petäjä, T., Aalto, P. P., Arshinov, M., Asmi, E., Baltensperger, U., Beddows, D. C. S.,

591   Beukes, J. P., Collins, D., Ding, A., Harrison, R. M., Henzing, B., Hooda, R., Hu, M., Hõrrak, U., Kivekäs, N., Komsaare,

592   K., Krejci, R., Kristensson, A., Laakso, L., Laaksonen, A., Leaitch, W. R., Lihavainen, H., Mihalopoulos, N., Németh,

593   Z., Nie, W., O'Dowd, C., Salma, I., Sellegri, K., Svenningsson, B., Swietlicki, E., Tunved, P., Ulevicius, V., Vakkari, V.,

594 Vana, M., Wiedensohler, A., Wu, Z., Virtanen, A. and Kulmala, M.: Global analysis of continental boundary layer new
595 particle formation based on long-term measurements, Atmos. Chem. Phys., 18(19), 14737–14756, doi:10.5194/acp-18-
596 14737-2018, 2018.

597 Ozon, M., Seppänen, A., Kaipio, J. P. and Lehtinen, K. E. J.: Retrieval of process rate parameters in the general dynamic
598 equation for aerosols using Bayesian state estimation, Geosci. Model Dev. Discuss., 2020, 1–32, doi:10.5194/gmd-2020-
599 236, 2020.

600 Pichelstorfer, L., Stolzenburg, D., Ortega, J., Karl, T., Kokkola, H., Laakso, A., Lehtinen, K. E. J., Smith, J. N., McMurry,
601 P. H. and Winkler, P. M.: Resolving nanoparticle growth mechanisms from size- and time-dependent growth rate analysis,
602 Atmos. Chem. Phys., 18(2), 1307–1323, doi:10.5194/acp-18-1307-2018, 2018.

603 Pope, C. A. and Dockery, D. W.: Health Effects of Fine Particulate Air Pollution: Lines that Connect, J. Air Waste
604 Manag., 56(6), 709–742, doi:10.1080/10473289.2006.10464485, 2006.

605 Sandu, A., Liao, W., Carmichael, G. R., Henze, D. K. and Seinfeld, J. H.: Inverse Modeling of Aerosol Dynamics Using
606 Adjoints: Theoretical   and   Numerical   Considerations,   Aerosol   Sci.   Tech.,   39(8),   677–694,
607 doi:10.1080/02786820500182289, 2005.

608 Seinfeld, J. and Pandis, S.: Atmospheric Chemistry and Physics: From Air Pollution to Climate Change, 3rd edition, 3rd
609 editio., Wiley., 2016.

610 Shcherbacheva, A., Balehowsky, T., Kubečka, J., Olenius, T., Helin, T., Haario, H., Laine, M., Kurtén, T. and Vehkamäki,
611 H.: Identification of molecular cluster evaporation rates, cluster formation enthalpies and entropies by Monte Carlo
612 method, Atmos. Chem. Phys. Discuss., 2020, 1–58, doi:10.5194/acp-2019-1036, 2020.

613 Shen, J., Shu, C. and Zhang, M.: High Resolution Schemes for a Hierarchical Size-Structured Model, SIAM J. Numer.
614 Anal., 45(1), 352–370, doi:10.1137/050638126, 2007.

615 Simon, M., Dada, L., Heinritzi, M., Scholz, W., Stolzenburg, D., Fischer, L., Wagner, A. C., Kürten, A., Rörup, B., He,
616 X.-C., Almeida, J., Baalbaki, R., Baccarini, A., Bauer, P. S., Beck, L., Bergen, A., Bianchi, F., Bräkling, S., Brilke, S.,
617 Caudillo, L., Chen, D., Chu, B., Dias, A., Draper, D. C., Duplissy, J., El-Haddad, I., Finkenzeller, H., Frege, C., Gonzalez-
618 Carracedo, L., Gordon, H., Granzin, M., Hakala, J., Hofbauer, V., Hoyle, C. R., Kim, C., Kong, W., Lamkaddam, H.,
619 Lee, C. P., Lehtipalo, K., Leiminger, M., Mai, H., Manninen, H. E., Marie, G., Marten, R., Mentler, B., Molteni, U.,
620 Nichman, L., Nie, W., Ojdanic, A., Onnela, A., Partoll, E., Petäjä, T., Pfeifer, J., Philippov, M., Quéléver, L. L. J.,
621 Ranjithkumar, A., Rissanen, M. P., Schallhart, S., Schobesberger, S., Schuchmann, S., Shen, J., Sipilä, M., Steiner, G.,
622 Stozhkov, Y., Tauber, C., Tham, Y. J., Tomé, A. R., Vazquez-Pufleau, M., Vogel, A. L., Wagner, R., Wang, M., Wang,
623 D. S., Wang, Y., Weber, S. K., Wu, Y., Xiao, M., Yan, C., Ye, P., Ye, Q., Zauner-Wieczorek, M., Zhou, X., Baltensperger,
624 U., Dommen, J., Flagan, R. C., Hansel, A., Kulmala, M., Volkamer, R., Winkler, P. M., Worsnop, D. R., Donahue, N.
625 M., Kirkby, J. and Curtius, J.: Molecular understanding of new-particle formation from alpha-pinene between -50 and
626 +25 °C, Atmos. Chem. Phys., 20(15), 9183–9207, doi:10.5194/acp-20-9183-2020, 2020.

627 Sipilä, M., Sarnela, N., Jokinen, T., Henschel, H., Junninen, H., Kontkanen, J., Richters, S., Kangasluoma, J., Franchin,
628 A., Peräkylä, O., Rissanen, M. P., Ehn, M., Vehkamäki, H., Kurten, T., Berndt, T., Petäjä, T., Worsnop, D., Ceburnis, D.,
629 Kerminen, V.-M., Kulmala, M. and O'Dowd, C.: Molecular-scale evidence of aerosol particle formation via sequential
630 addition of HIO3, Nature, 537, 532, doi:10.1038/nature19314, 2016.

631 Smolarkiewicz, P. K.: A fully multidimensional positive definite advection transport algorithm with small implicit
632 diffusion, J. Comput. Phys., 54(2), 325–362, doi:https://doi.org/10.1016/0021-9991(84)90121-9, 1984.

633 Stolzenburg, D., Steiner, G. and Winkler, P. M.: A DMA-train for precision measurement of sub-10 nm aerosol dynamics,

634   Atmos. Meas. Tech., 10(4), 1639–1651, doi:10.5194/amt-10-1639-2017, 2017.

635   Stolzenburg, D., Fischer, L., Vogel, A. L., Heinritzi, M., Schervish, M., Simon, M., Wagner, A. C., Dada, L., Ahonen, L.

636   R., Amorim, A., Baccarini, A., Bauer, P. S., Baumgartner, B., Bergen, A., Bianchi, F., Breitenlechner, M., Brilke, S.,

637   Buenrostro Mazon, S., Chen, D., Dias, A., Draper, D. C., Duplissy, J., El Haddad, I., Finkenzeller, H., Frege, C., Fuchs,

638   C., Garmash, O., Gordon, H., He, X., Helm, J., Hofbauer, V., Hoyle, C. R., Kim, C., Kirkby, J., Kontkanen, J., Kürten,

639   A., Lampilahti, J., Lawler, M., Lehtipalo, K., Leiminger, M., Mai, H., Mathot, S., Mentler, B., Molteni, U., Nie, W.,

640   Nieminen, T., Nowak, J. B., Ojdanic, A., Onnela, A., Passananti, M., Petäjä, T., Quéléver, L. L. J., Rissanen, M. P.,

641   Sarnela, N., Schallhart, S., Tauber, C., Tomé, A., Wagner, R., Wang, M., Weitz, L., Wimmer, D., Xiao, M., Yan, C., Ye,

642   P., Zha, Q., Baltensperger, U., Curtius, J., Dommen, J., Flagan, R. C., Kulmala, M., Smith, J. N., Worsnop, D. R., Hansel,

643   A., Donahue, N. M. and Winkler, P. M.: Rapid growth of organic aerosol nanoparticles over a wide tropospheric

644   temperature range, P. Nat. Acad. Sci. USA, 115(37), 9122–9127, doi:10.1073/pnas.1807604115, 2018.

645   Stolzenburg, D., Simon, M., Ranjithkumar, A., Kürten, A., Lehtipalo, K., Gordon, H., Ehrhart, S., Finkenzeller, H.,

646   Pichelstorfer, L., Nieminen, T., He, X.-C., Brilke, S., Xiao, M., Amorim, A., Baalbaki, R., Baccarini, A., Beck, L.,

647   Bräkling, S., Caudillo Murillo, L., Chen, D., Chu, B., Dada, L., Dias, A., Dommen, J., Duplissy, J., El Haddad, I., Fischer,

648   L., Gonzalez Carracedo, L., Heinritzi, M., Kim, C., Koenig, T. K., Kong, W., Lamkaddam, H., Lee, C. P., Leiminger, M.,

649   Li, Z., Makhmutov, V., Manninen, H. E., Marie, G., Marten, R., Müller, T., Nie, W., Partoll, E., Petäjä, T., Pfeifer, J.,

650   Philippov, M., Rissanen, M. P., Rörup, B., Schobesberger, S., Schuchmann, S., Shen, J., Sipilä, M., Steiner, G., Stozhkov,

651   Y., Tauber, C., Tham, Y. J., Tomé, A., Vazquez-Pufleau, M., Wagner, A. C., Wang, M., Wang, Y., Weber, S. K., Wimmer,

652   D., Wlasits, P. J., Wu, Y., Ye, Q., Zauner-Wieczorek, M., Baltensperger, U., Carslaw, K. S., Curtius, J., Donahue, N. M.,

653   Flagan, R. C., Hansel, A., Kulmala, M., Lelieveld, J., Volkamer, R., Kirkby, J. and Winkler, P. M.: Enhanced growth rate

654   of atmospheric particles from sulfuric acid, Atmos. Chem. Phys., 20(12), 7359–7372, doi:10.5194/acp-20-7359-2020,

655   2020.

656   Stolzenburg, M. R. and McMurry, P. H.: Equations Governing Single and Tandem DMA Configurations and a New

657   Lognormal Approximation to the Transfer Function, Aerosol Sci. Tech., 42, 421–432, doi:10.1080/02786820802157823,

658   2008.

659   Tauber, C., Schmoll, D., Gruenwald, J., Brilke, S., Wlasits, P. J., Winkler, P. M. and Wimmer, D.: Characterization of a

660   Non-Thermal Plasma Source for the Use as a Mass Spec Calibration Tool and Non-Radioactive Aerosol Charger, Atmos.

661   Meas. Tech., 13(11), 5993–6006, doi:10.5194/amt-13-5993-2020, 2020.

662   Tröstl, J., Chuang, W. K., Gordon, H., Heinritzi, M., Yan, C., Molteni, U., Ahlm, L., Frege, C., Bianchi, F., Wagner, R.,

663   Simon, M., Lehtipalo, K., Williamson, C., Craven, J. S., Duplissy, J., Adamov, A., Almeida, J., Bernhammer, A.-K.,

664   Breitenlechner, M., Brilke, S., Dias, A., Ehrhart, S., Flagan, R. C., Franchin, A., Fuchs, C., Guida, R., Gysel, M., Hansel,

665   A., Hoyle, C. R., Jokinen, T., Junninen, H., Kangasluoma, J., Keskinen, H., Kim, J., Krapf, M., Kürten, A., Laaksonen,

666   A., Lawler, M., Leiminger, M., Mathot, S., Möhler, O., Nieminen, T., Onnela, A., Petäjä, T., Piel, F. M., Miettinen, P.,

667   Rissanen, M. P., Rondo, L., Sarnela, N., Schobesberger, S., Sengupta, K., Sipilä, M., Smith, J. N., Steiner, G., Tomè, A.,

668   Virtanen, A., Wagner, A. C., Weingartner, E., Wimmer, D., Winkler, P. M., Ye, P., Carslaw, K. S., Curtius, J., Dommen,

669   J., Kirkby, J., Kulmala, M., Riipinen, I., Worsnop, D. R., Donahue, N. M. and Baltensperger, U.: The role of low-volatility

670   organic compounds in initial particle growth in the atmosphere, Nature, 533, 527–531, doi:10.1038/nature18271, 2016.

671   Twomey, S.: Pollution and the planetary albedo, Atmos. Environ., 8(12), 1251–1256, doi:https://doi.org/10.1016/0004-

672   6981(74)90004-3, 1974.

673   Verheggen, B. and Mozurkewich, M.: An inverse modeling procedure to determine particle growth and nucleation rates

Atmospheric
Chemistry
and Physics
Discussions
Open Access
EGU

674   from measured aerosol size distributions, Atmos. Chem. Phys., 6(10), 2927–2942, doi:10.5194/acp-6-2927-2006, 2006.

675   Viskari, T., Asmi, E., Kolmonen, P., Vuollekoski, H., Petäjä, T. and Järvinen, H.: Estimation of aerosol particle number

676   distributions with Kalman Filtering – Part 1: Theory, general aspects and statistical validity, Atmos. Chem. Phys., 12(24),

677   11767–11779, doi:10.5194/acp-12-11767-2012, 2012.

678   Wiedensohler, A.: An approximation of the bipolar charge distribution for particles in the submicron size range, J. Aerosol

679   Sci., 19(3), 387–389, doi:10.1016/0021-8502(88)90278-9, 1988.

680   Wlasits, P. J., Stolzenburg, D., Tauber, C., Brilke, S., Schmitt, S. H., Winkler, P. M. and Wimmer, D.: Counting on

681   chemistry: laboratory evaluation of seed-material-dependent detection efficiencies of ultrafine condensation particle

682   counters, Atmos. Meas. Tech., 13(7), 3787–3798, doi:10.5194/amt-13-3787-2020, 2020.

683   Wolfenbarger, J. K. and Seinfeld, J. H.: Inversion of aerosol size distribution data, J. Aerosol Sci., 21(2), 227–247,

684   doi:https://doi.org/10.1016/0021-8502(90)90007-K, 1990.

685